PAPER

Check for updates

Cite this: DOI: 10.1039/d1ta00468a

Uniform synthesis of palladium species confined in a small-pore zeolite *via* full ion-exchange investigated by cryogenic electron microscopy†

Yongwoo Kim,‡[a] Jongbaek Sung, [iD] ‡[ab] Sungsu Kang,[ab] Jaeha Lee,[a] Min-Ho Kang,[ab] Sungha Hwang, [iD] [a] Hayoung Park,[ab] Joodeok Kim,[ab] Younhwa Kim,[ab] Eunwon Lee,[a] Gyeong-Su Park,[c] Do Heui Kim [iD] *[a] and Jungwon Park [iD] *[ab]

Finely dispersing noble metal species with high phase homogeneity in zeolites is crucial to develop an efficient catalyst. However, for palladium-impregnated zeolites, fully utilizing active palladium species in small-pore zeolites with high dispersion is challenging despite the establishment of a general synthetic approach of ion-exchange and subsequent thermal treatment to generate encapsulated nanoparticles. Herein, we achieve full dispersion of isolated Pd^{2+} ions in a small-pore SSZ-13 zeolite *via* a controlled ion-exchange process, and successfully generate uniformly dispersed nano-sized PdO clusters in SSZ-13 supported by mechanistic understanding of nanoparticle growth. Direct investigation *via* cryogenic electron microscopy and ultramicrotomy allows the successful artifact-free imaging of electron-beam-sensitive zeolite-based catalysts, and reveals that the formation of nano-sized PdO clusters during thermal treatment is governed by the rapid nucleation and suppressed particle growth in a confined space. Through fully utilizing active Pd species in SSZ-13 by controlled ion-exchange and rationalized thermal treatment, enhanced catalytic performances toward a passive NO_x adsorber and CH_4 combustion are achieved.

Introduction

Palladium species encapsulated small-pore zeolites have attracted significant attention owing to their distinctive catalytic performances.[1–5] Compared to other zeolites with a larger pore size, small-pore zeolites can stabilize nano-sized noble metal species to show comparably high stability, which is crucial for catalytic reactions under realistic conditions.[3,6–8] Particularly, applications of Pd-impregnated small-pore zeolite catalysts for after-treatment and hydrogen generation have been successfully demonstrated.[3,6,7] In these cases, various Pd phases such as isolated Pd^{2+} ions, Pd, and PdO can exist in the zeolite, all of which show different catalytic activities depending on the reaction.[3–5,7,9] For example, isolated Pd^{2+} ions are active for passive NO_x adsorbers (PNAs),[5,9] while most catalytic reactions including catalytic combustion of CH_4 require highly dispersed

Pd or PdO nanoparticles for high catalytic activity.[7,10] Therefore, generating confined Pd species with high dispersion and with a homogeneous phase in small-pore zeolites is necessary to efficiently utilize the expensive Pd for catalytic applications.

Among various synthetic methods to locate noble metal species in zeolites,[11–14] introducing noble metal precursors by ion-exchanging them with cationic species of zeolites and subsequently generating nanoparticles *via* thermal treatment is recognized as a practical method.[1] However, in general, poor controllability inherent in both ion-exchange and thermal treatment hinders the efficient utilization of Pd in small-pore zeolites. The unwanted adsorption of precursors on the external surface of the zeolite occurs concurrently with ion-exchange at the internal channel of the zeolite, resulting in the formation of large-sized particles.[15,16] For small-pore zeolites such as SSZ-13 (channel size of 0.38×0.38 nm^2), ion-exchange is further suppressed by the limited accessibility of the zeolite channels, causing a serious problem toward achieving high ion-exchange efficiency.[2,17] Furthermore, the formation of nanoparticles from isolated Pd^{2+} ions during thermal treatment is complicated by multiple processes including the nucleation from the isolated Pd^{2+} ions and the confined growth of nanoparticles in the nano-sized pores of zeolite, limiting the formation of highly dispersed active Pd species with a homogeneous phase. Direct observation of nanoparticles confined in the zeolite, if enabled, can facilitate the optimization of

[a]School of Chemical and Biological Engineering and Institute of Chemical Process, Seoul National University, Seoul 08826, Republic of Korea. E-mail: jungwonpark@snu.ac.kr; dohkim@snu.ac.kr

[b]Center for Nanoparticle Research, Institute for Basic Science (IBS), Seoul 08826, Republic of Korea

[c]Department of Materials Science and Engineering and Research Institute of Advanced Materials, Seoul National University, Seoul 08826, Republic of Korea

† Electronic supplementary information (ESI) available. See DOI: 10.1039/d1ta00468a

‡ Y. Kim and J. Sung contributed equally to this work.

complex particle growth in this system. Transmission electron microscopy (TEM) is a promising method that ensures microscopic imaging with sufficient spatial resolution,[18–20] but the zeolites are generally electron-beam sensitive, exhibiting a collapse of microstructures when they are exposed to an electron-beam used in typical TEM.[21–23] In particular, small-pore zeolites such as SSZ-13 are vulnerable to electron-beam-induced degradation due to their weak mechanical strength and low framework density.[24,25] Furthermore, the deteriorated image resolution of the nanoparticles embedded in the zeolite also hinders the application of conventional TEM in resolving particle formation in zeolites.[21,22] Hence, understanding the ion-exchange process and the detailed growth behavior of Pd species in the zeolite, ideally by direct observation with an advanced TEM technique, is required to achieve the efficient synthesis of highly dispersed Pd species with high phase homogeneity for catalytic applications.

Herein, the fully isolated Pd^{2+} ions in SSZ-13 is synthesized by achieving full ion-exchange efficiency. Thereafter, the generation and growth behavior of the nano-sized PdO clusters in SSZ-13 are directly investigated through a combination of cryogenic scanning transmission electron microscopy (cryo-STEM) and ultramicrotomy with minimized electron-beam induced damage. The obtained mechanistic understanding allows successful preparation of uniformly dispersed nano-sized PdO clusters confined in a small-pore SSZ-13 zeolite from fully isolated Pd^{2+} ions, by controlling the thermal treatment that induces rapid nucleation and suppressed nanoparticle growth. The enhanced PNA and CH_4 combustion performances highlight the importance of our method comprising full ion-exchange efficiency and rationalized nanoparticle growth for Pd-impregnated zeolite catalysts.

Result and discussion

SSZ-13 with a low Si/Al ratio of 4.5, determined by ^{29}Si magic angle spinning nuclear magnetic resonance (Si-MAS-NMR), was synthesized for ensuring a sufficient amount of Al-sites to stabilize isolated Pd^{2+} ions (Fig. S1 and Table S1†).[26,27] The typical CHA-structure of synthesized SSZ-13 is confirmed by X-ray diffraction (XRD) (Fig. S2†). The extent of isolated Pd^{2+} ions in SSZ-13 is affected in the ion-exchange process between the Pd precursor and SSZ-13 in the aqueous solution. We prepared various Pd-exchanged SSZ-13 samples using different combinations of water-soluble Pd precursors ($Pd(NO_3)_2$ and $Pd(NH_3)_4Cl_2$) and zeolite-forms (H-SSZ-13 and NH₄-SSZ-13) (Experimental section and Table S2†). Among the as-prepared samples, only the sample prepared with $Pd(NH_3)_4Cl_2$ and NH₄-SSZ-13 does not show any clustered Pd precursors on the external surface of the zeolite, whereas a large amount of clustered Pd precursors are commonly observed on the external surface of the zeolite for samples prepared with either $Pd(NO_3)_2$ or H-SSZ-13, as shown in TEM images in Fig. 1a (Fig. S3†). The state of the Pd-ionic complex in the precursor solution immensely affects the dispersion of Pd precursors in SSZ-13, because the Pd-ionic complex is exchanged with H^+ or NH_4^+ of SSZ-13. The Pd-ionic complex in the $Pd(NH_3)_4Cl_2$ solution

exists as a positively charged form of $[Pd(NH_3)_4]^{2+}$,[28] whereas $Pd(NO_3)_2$ solution contains negatively charged species,[29] as confirmed by the UV-vis spectra in Fig. S4.† During ion-exchange in the aqueous solution, the negative charge of the Pd-ionic complex in $Pd(NO_3)_2$ solution hinders diffusion into the negatively charged zeolite channel and ion-exchange with positively charged H^+ or NH_4^+.[11] In addition, Pd-hydrate complexes can exist in the $Pd(NO_3)_2$ solution, and prevent ion-exchange due to its large hydrated radius.[30] The XPS analysis of the as-prepared samples before the calcination step also indicate that the surface Pd/Al atomic ratios of samples prepared with $Pd(NO_3)_2$ are much higher than those of samples prepared with $Pd(NH_3)_4Cl_2$, as listed in Table S3.† This indicates that the Pd-ionic complex in $Pd(NH_3)_4Cl_2$ solution can penetrate into SSZ-13 much better than that in $Pd(NO_3)_2$ solution. Furthermore, the similar level between the surface Pd/Al atomic ratios and the bulk Pd/Al atomic ratios of the samples prepared with $Pd(NH_3)_4Cl_2$ demonstrates that the Pd precursors were well-distributed through SSZ-13, but not concentrated on the surface (Table S3†). The zeolite-form also affects the ion-exchange efficiency. The ion-exchange equilibrium between the Pd^{2+} ions and H-form (or NH₄-form) zeolite is as follows:

$$Pd^{2+} + 2Al–OH \ (or \ 2Al–ONH_4) \leftrightarrow 2(Al–O)Pd + 2H^+ \ (or \ 2NH_4^+)$$
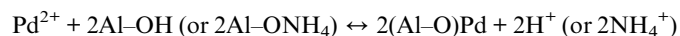
Based on Le Chatelier's principle, the acidic environment in the zeolite limits the shift of the equilibrium to the right due to the formation of H^+.[5] Meanwhile, since the formation of NH_4^+ is less affected by the acidic environment, the ion-exchange of the NH₄-form zeolite is facilitated.[31]

The calcination step that decomposes the ion-exchanged Pd precursors also affects the extent of isolated Pd^{2+} ions. The cryogenic H_2 temperature programmed reduction (cryo-H_2-TPR) profile of Pd-exchanged SSZ-13 samples evaluates the extent of isolated Pd^{2+} ions in SSZ-13 after calcination with a ramping rate of 10 °C min⁻¹, as shown in Fig. 1b.[30,32,33] The broad peak at approximately 100 °C arises from the reduction of the isolated Pd^{2+} ions, whereas the sharp peak at approximately 0 °C originates from the reduction of PdO that is not ion-exchanged.[30,32,33] All Pd-exchanged SSZ-13 samples contain a large peak of isolated Pd^{2+} ions due to the sufficient amount of Al-sites, whereas the peak intensity of PdO varies according to a combination of precursors and zeolite-forms. Pd-exchanged SSZ-13 prepared using $Pd(NH_3)_4Cl_2$ and NH₄-SSZ-13 (the sample with a negligible amount of clustered Pd precursors in Fig. 1a) contains a trace amount of PdO. Conversely, a notable amount of PdO was observed in samples prepared using either $Pd(NO_3)_2$ or H-SSZ-13, indicating that the application of $Pd(NH_3)_4Cl_2$ and NH₄-SSZ-13 provides the highest ion-exchange efficiency.

To maintain the full ion-exchange efficiency of Pd^{2+} ions even after the calcination step, the Pd-exchanged SSZ-13 sample prepared with $Pd(NH_3)_4Cl_2$ and NH₄-SSZ-13 were calcined with different ramping rates. The cryo-H_2-TPR profiles of these samples demonstrate that the intensity of the PdO peak increases with increasing the ramping rate for calcination (Fig. S5†). According to the solid-state UV-vis analysis in Fig. 1c, the Pd species in the Pd-exchanged SSZ-13 prepared using
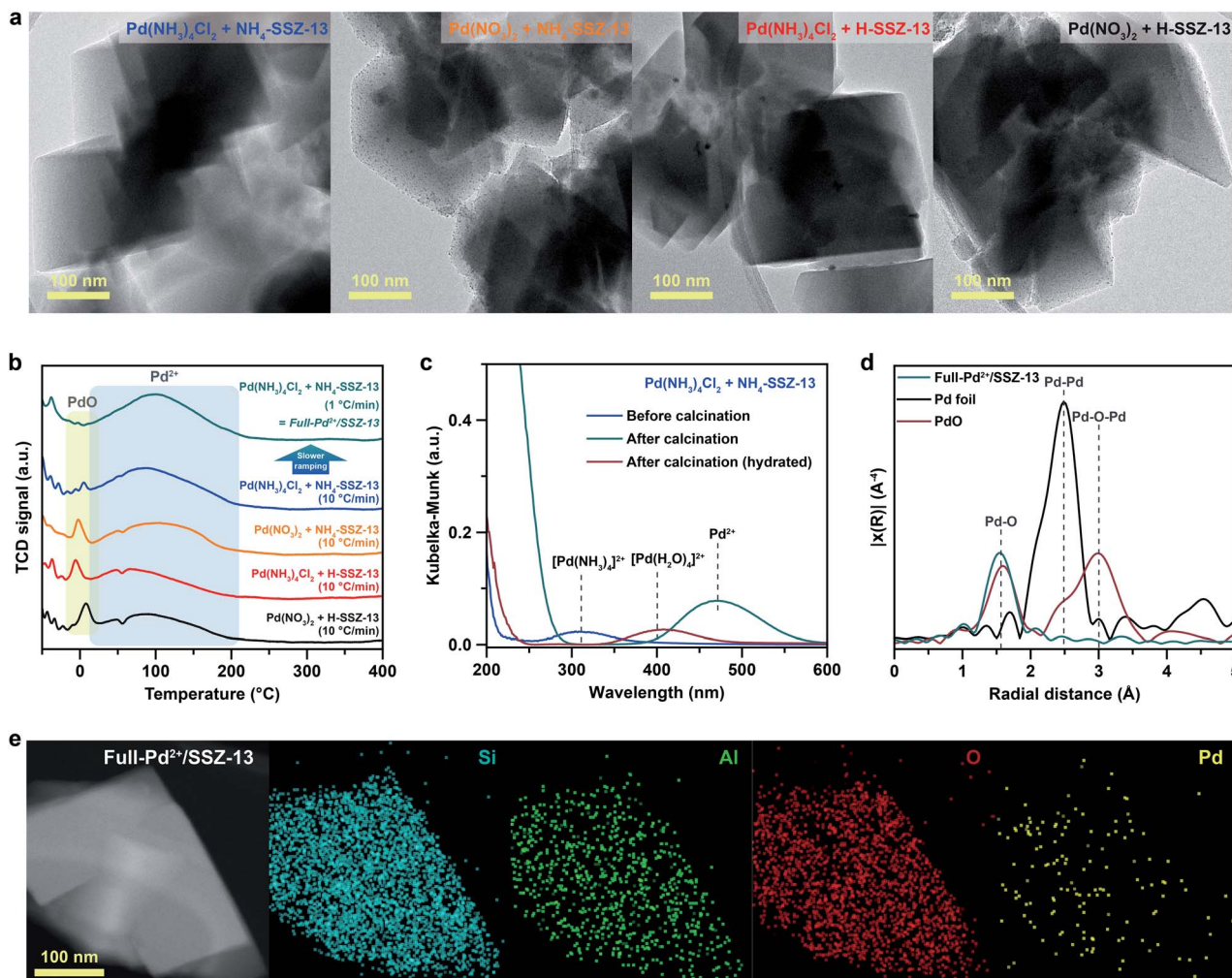
Fig. 1 (a) TEM images of Pd-exchanged SSZ-13 samples prepared with different combinations of Pd precursors and zeolite-forms, before calcination. (b) Cryo-H_2-TPR profiles of the Pd-exchanged SSZ-13 samples prepared using different combinations of precursors, zeolite-forms, and ramping rates for calcination. (c) Solid-state UV-vis spectra of Pd-exchanged SSZ-13 samples prepared with $Pd(NH_3)_4Cl_2$ and NH_4-SSZ-13, before and after calcination. (d) k^3-weighted Fourier-transformed EXAFS spectra of Full-Pd^{2+}/SSZ-13, Pd foil, and PdO reference. (e) Cryogenic HAADF-STEM image and EDS maps of Full-Pd^{2+}/SSZ-13.

$Pd(NH_3)_4Cl_2$ and NH_4-SSZ-13 exist as $Pd(NH_3)_4^{2+}$ before the calcination, indicating that the calcination step decomposes $Pd(NH_3)_4^{2+}$ species into isolated Pd^{2+} ions. However, when the ramping rate for calcination is too fast, the unstable Pd^{2+} ions, decomposed from $Pd(NH_3)_4^{2+}$ species, can assemble to form PdO particles instead of interacting with Al-sites of SSZ-13. Hence, it can be deduced that the slow ramping rate is required to ensure sufficient time for the Pd^{2+} ions to be stabilized at Al-sites thereby suppressing the agglomeration of the Pd^{2+} ions. We also note that the redispersion of Pd species during the calcination can contribute to generating isolated Pd^{2+} ions,[34] but for the case of the Pd-exchanged SSZ-13 sample prepared with $Pd(NH_3)_4Cl_2$ and NH_4-SSZ-13, the redispersion of surface Pd species into the internal zeolite was less noticeable since the Pd species had already been well-distributed through the SSZ-13 (Fig. 1b and Table S3†).

Based on the understanding of the formation of isolated Pd^{2+} ions through ion-exchange in aqueous solution and the

subsequent calcination step, Pd-exchanged SSZ-13 with full ion-exchange efficiency (denoted as Full-Pd^{2+}/SSZ-13) was prepared using $Pd(NH_3)_4Cl_2$ and NH_4-SSZ-13, and applying a slow ramping rate of 1 °C min^{-1} during calcination. The fully isolated Pd^{2+} ions in the Full-Pd^{2+}/SSZ-13 was confirmed by the absence of the PdO peak in the cryo-H_2-TPR profile, as shown in Fig. 1b. In addition, the extended X-ray absorption fine structure (EXAFS) spectrum of Full-Pd^{2+}/SSZ-13 demonstrates one major peak at a radial distance of 1.6 Å corresponding to the Pd–O bond, as displayed in Fig. 1d. The absence of the Pd–Pd and Pd–O–Pd peaks in the EXAFS spectrum indicates that the Pd species thoroughly exists as isolated Pd^{2+} ions.[5,30,35] The TEM image of Full-Pd^{2+}/SSZ-13 demonstrates none of the PdO particles on the external surface of the zeolite, whereas the agglomerated PdO particles are present in other Pd-exchanged SSZ-13 samples with insufficient ion-exchange efficiency, as shown in Fig. S6.† The high-angle annular dark-field scanning transmission electron microscopy (HAADF-STEM) image and

energy dispersive X-ray spectroscopy (EDS) maps of Full-Pd^{2+}/SSZ-13 confirmed the presence of well-dispersed Pd^{2+} ions, as illustrated in Fig. 1e. We emphasize that the full ion-exchange efficiency of Pd^{2+} ions in Full-Pd^{2+}/SSZ-13 can be achieved when the choice of precursor combination and the ramping rate for calcination are optimized (Fig. S7†).

In order to control the generation of nano-sized PdO clusters from isolated Pd^{2+} ions, Full-Pd^{2+}/SSZ-13 was treated with H_2 at 700 °C for different times of 1, 5, 10, and 60 min. Subsequently, the catalysts were gently oxidized to transform the metallic Pd into PdO, an active species for CH_4 combustion. Note that the differences in the crystallinity and the Brunauer–Emmett–Teller (BET) surface area between the thermal-treated Pd/SSZ-13 catalysts with different H_2 treatment times were negligible (Fig. S8†).

Cryo-STEM coupled with ultramicrotomy was utilized to directly observe the generated Pd species confined in the SSZ-13 zeolite. Microscopic observation of the nano-sized Pd species located at the internal site of the zeolite is usually hindered due to the deteriorated image resolution caused by the surrounding zeolite particle. In addition, both the metal species and the zeolites are prone to electron-beam induced damage, resulting in unwanted agglomeration of metal species and radiolysis of the zeolite during TEM imaging.[5,22,25] In particular, since the SSZ-13 used in this study has a relatively low framework density of 15.1 T/1000 Å³,[36] and also has high Al content that easily traps water,[23,30] the structural degradation of SSZ-13 zeolite during electron-beam irradiation is severe during conventional TEM imaging (Movie S1†).[21] To overcome these obstacles, we ultra-microtomed Pd/SSZ-13 samples into ~50 nm thick sections to reveal the internal Pd species in the zeolite.[37,38] Thereafter, to minimize the electron-beam induced damage during imaging while obtaining high Z-contrast, the ultramicrotomed sections were observed under the STEM mode at a cryogenic temperature of −180 °C.[25,39–41] The overall process of ultramicrotomy and cryo-STEM imaging is illustrated in Fig. 2a and b. The undesired electron-beam effect is further avoided by applying minimal scanning during cryo-STEM imaging. We emphasize that this method ensures the observation of nano-sized clusters confined in the internal site of the high-Al and small-pore zeolite without structural ambiguity, while preventing electron-beam induced artifacts (Fig. S9 and Movie S2†).

The cryo-STEM imaging of the thermal-treated Pd/SSZ-13 catalysts with different H_2 treatment times elucidates the structural evolution of the nano-sized PdO clusters in the zeolite during thermal treatment. Owing to the full ion-exchange and the successful minimization of the electron-beam induced damage, the Pd species are unobservable in the cryo-STEM images of the ultramicrotomed Full-Pd^{2+}/SSZ-13 before the thermal treatment (Fig. S10 and S11†).[5] The observation of the well-dispersed nano-sized PdO clusters in the thermal-treated Pd/SSZ-13 catalysts indicates that thermal treatment successfully generated nano-sized PdO clusters confined in SSZ-13 (Fig. 2c–f). Furthermore, the majority of the nano-sized PdO clusters are observed in the interior site of the ultramicrotomed Pd/SSZ-13 sections, indicating that the nano-sized PdO clusters predominantly exist in the internal pores of the SSZ-13 zeolite.[42]

However, dispersion of the generated nano-sized PdO clusters varied with the H_2 treatment time, as shown in Fig. 2c–f. We obtained the size distribution of nano-sized PdO clusters in each sample by quantifying 500 nanoparticles locating at the internal pores of zeolite without ambiguity of their locations, such as the external surface of the zeolite, as shown in Fig. 2g–j. Notably, the average particle size of a 1 min H_2-treated sample is 1.70 ± 0.54 nm and the values are almost stable for 5 min and 10 min of H_2 treatment with slightly reduced values of 1.62 ± 0.42 nm and 1.67 ± 0.46 nm, respectively. The average particle size slowly increases to 2.02 ± 0.65 nm after 60 min of H_2 treatment owing to particle growth by the sintering process, which is not as significant as expected for the sintering in typical supported catalyst systems.[43,44] We note that the average particle sizes in Fig. 2g–j are similar to the average pore diameter of SSZ-13 (1.8 nm), obtained from Ar adsorption–desorption measurements (Fig. S12 and Table S1†). This non-typical growth behavior of the PdO nanoparticles is also depicted in the overall sharpness of size distribution, as indicated by the kurtosis value that statistically represents the heaviness of tail in the size distribution (Fig. 2g–j). Although the size distributions of Pd/SSZ-13 treated with H_2 for 1 min and 60 min are broad, indicated by a relatively low kurtosis value of 0.839 and 0.859 respectively, those treated with H_2 for 5 min and 10 min show focused size distributions with a high kurtosis value above 2.7.

Nanoparticle growth in supported catalyst systems generally shows an increase in both the average size and the broadness of size distribution, mainly attributed to Ostwald ripening.[45,46] However, the nanoparticle growth observed in Fig. 2g–j shows a size-focusing behavior at moderate H_2 treatment times of 5 min and 10 min. The cryo-H_2-TPR profiles of the thermal-treated Pd/SSZ-13 catalysts indicate that a significant amount of Pd^{2+} ions remained after 1 min of H_2 treatment and disappeared after 5 min, as represented in Fig. 3a. These observations imply that the nucleation of isolated Pd^{2+} ions rapidly occurs and reaches the full conversion of Pd^{2+} ions during the first few minutes of H_2 treatment. In our study, the observed growth begins from Full-Pd^{2+}/SSZ-13 with a high concentration of well-dispersed isolated Pd^{2+} ions, and therefore, homogeneous nucleation of isolated Pd^{2+} ions is likely to occur and the growth pattern deviates from that of typical supported catalyst systems. Furthermore, the subsequent growth of the generated PdO nanoparticles is relatively sluggish by showing only a 0.32 nm increase in the average size from 1 min to 60 min of H_2 treatment (Fig. 2g and j). Such suppressed nanoparticle growth behaviour would be attributed to the confined environment by the surrounding zeolite, because our thermal treatment includes harsh reduction conditions that would otherwise cause severe Pd sintering.[47–49] Therefore, combining the effect of rapid nucleation and suppressed nanoparticle growth, the generation of nano-sized PdO clusters with high size-uniformity was achieved by a H_2 treatment of 5 min. Note that the rapid nucleation and size-focusing behavior is also observed from nanoparticle growth that includes a burst nucleation of monomers after overcoming the critical monomer concentrations.[50,51]
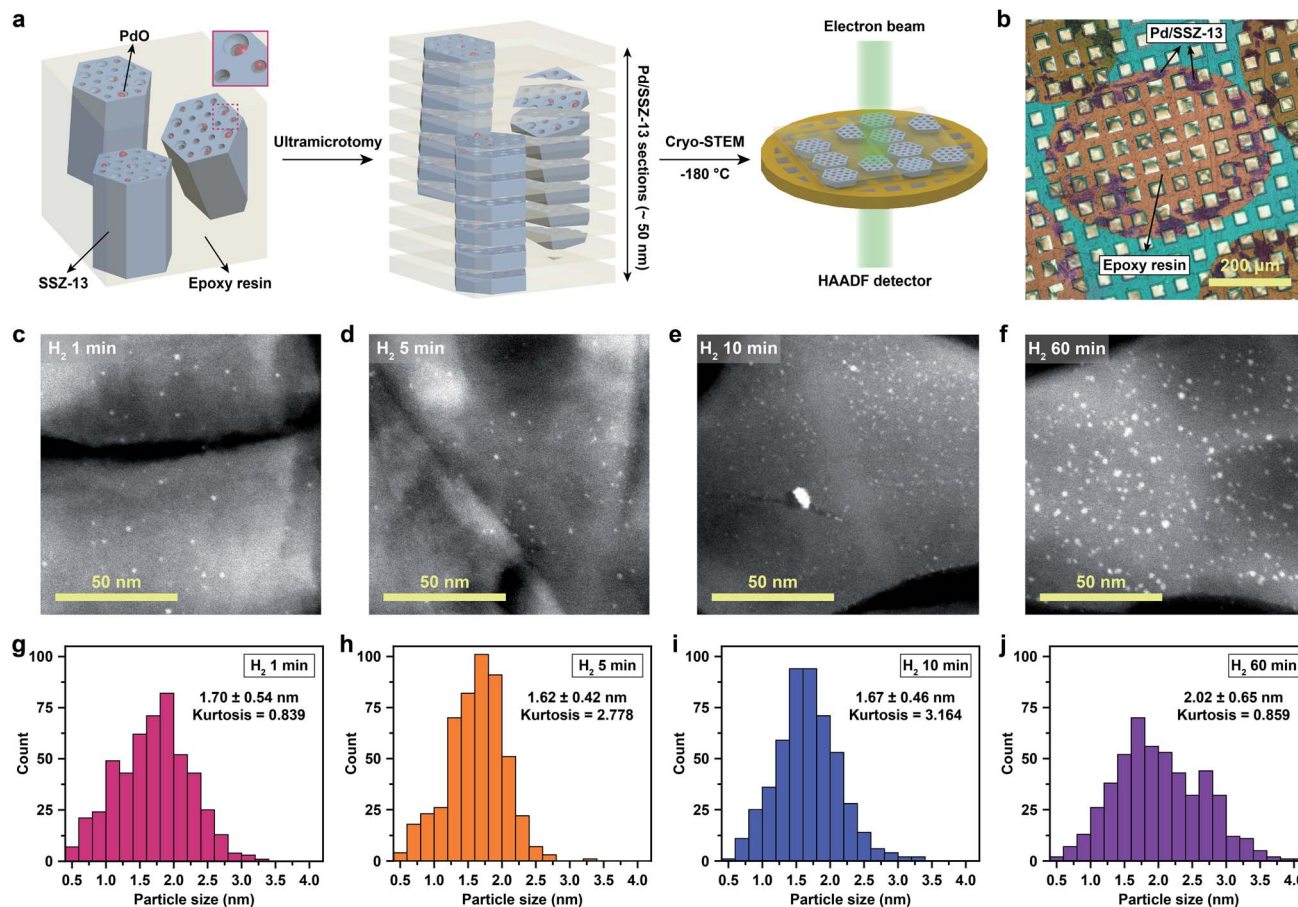
Fig. 2 (a) Illustration of ultramicrotomy and cryo-STEM imaging. (b) Optical microscope image of the ultramicrotomed Pd/SSZ-13 catalyst on the TEM grid. (c)–(f) Representative cryo-STEM images of thermal-treated Pd/SSZ-13 catalysts with H_2 treatment times of (c) 1 min, (d) 5 min, (e) 10 min, and (f) 60 min. (g)–(j) Size distribution of the nano-sized PdO clusters for the thermal-treated Pd/SSZ-13 catalysts with H_2 treatment times of (g) 1 min, (h) 5 min, (i) 10 min, and (j) 60 min.

We further confirmed that the synthesis process with full ion-exchange and an optimized H_2 treatment time of 5 min ensures the minimized generation of different Pd phases at unwanted locations other than the internal pore sites of the zeolite, thus resulting in a formation of nano-sized PdO clusters

with high phase homogeneity. The inhomogeneity of PdO was observed for the thermal-treated Pd/SSZ-13 catalysts with 10 min and 60 min of H_2 treatment, as indicated by the bimodal PdO peak in the cryo-H_2-TPR profiles in Fig. 3a. The X-ray absorption near edge structure (XANES) spectra of most of the
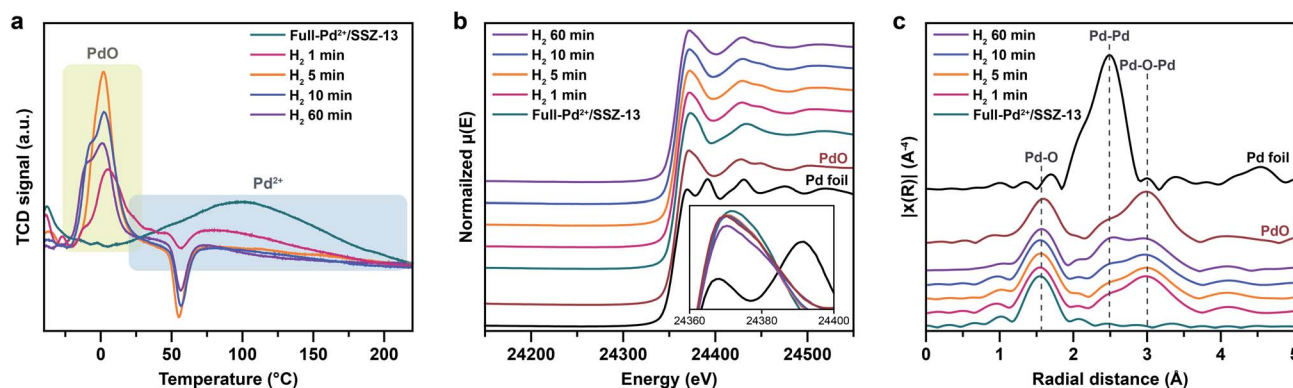

Fig. 3 (a) Cryo-H_2-TPR profiles, (b) normalized XANES spectra and (c) k^3-weighted Fourier-transformed EXAFS spectra of Full-Pd^{2+}/SSZ-13 and thermal-treated Pd/SSZ-13 catalysts with different H_2 treatment times.

thermal-treated Pd/SSZ-13 catalysts were similar to those of the PdO reference, whereas the thermal-treated Pd/SSZ-13 catalyst with 60 min of H_2 treatment was partially oxidized, as indicated by the reduced white line intensity in Fig. 3b. A consistent result was shown in the EXAFS spectra demonstrated in Fig. 3c. The thermal-treated Pd/SSZ-13 catalysts with 1 min and 5 min of H_2 treatment exhibited an atomic structure similar to that of the PdO reference, whereas those with further H_2 treatment show development of the Pd–Pd peak at approximately 2.5 Å, particularly for the Pd/SSZ-13 catalyst with 60 min of H_2 treatment. In addition, the cryo-STEM images of ultramicrotomed Pd/SSZ-13 indicate the existence of internal voids, as shown in Fig. 4a. Along with the external surface of the zeolite, these internal voids inherently existing in SSZ-13 can serve as agglomeration sites for Pd species during thermal treatment, resulting in the gradual development of large-sized internal Pd species with extended H_2 treatment times (Fig. S13†). We suspect that the partially oxidized Pd species are formed at the internal void where full oxidation of Pd can be suppressed due to limited volumetric expansion of large-sized Pd species. Indeed, the aberration-corrected TEM analysis of the internal void species revealed that different phases such as Pd and PdO_2,

thermodynamically unfavorable phases in an oxidative environment, coexist along with PdO at this site, as illustrated in Fig. 4b and c (Fig. S14 and S15†).[52–54] However, a unimodal PdO peak in the cryo-H_2-TPR profile and the negligible development of Pd species at internal voids were observed for thermal-treated Pd/SSZ-13 catalyst prepared from Full-Pd^{2+}/SSZ-13 and with 5 min of H_2 treatment, as demonstrated in Fig. 3a and S12.† Consequently, only the sample prepared with full ion-exchange efficiency and optimized H_2 treatment of 5 min enables the uniform generation of nano-sized PdO clusters with high phase homogeneiety.

The PNA and CH_4 combustion performances of diverse Pd/SSZ-13 catalysts consisting either isolated Pd^{2+} ions or nano-sized PdO clusters are evaluated to elucidate the advantage of full ion-exchange efficiency and rationalized thermal treatment. Since the isolated Pd^{2+} ions are active to adsorb NO_x, the PNA ability of the Pd/SSZ-13 catalysts before the thermal treatment was tested. Among the various samples prepared with different combinations of precursors, zeolite-forms, and ramping rates for calcination, Full-Pd^{2+}/SSZ-13 demonstrates the highest PNA ability, as this catalyst fully utilizes Pd species as isolated Pd^{2+} ions (Fig. 5a). Specifically, the amount of NO adsorbed on Full-Pd^{2+}/SSZ-13 is 68.2 μmol g_{cat}^{-1}, corresponding to 0.8 NO/Pd ratio. This is a comparably high value, as demonstrated in our previous research.[30] It should be noted that CO was added in a reactant feed since CO facilitates the adsorption of NO on Pd/SSZ-13 by forming NO–Pd–CO complexes[41] (Fig. S16†). Meanwhile, CH_4 hardly adsorbed on Pd/SSZ-13 (Fig. S16†). Meanwhile, the CH_4 combustion activity of Full-Pd^{2+}/SSZ-13 and the thermal-treated Pd/SSZ-13 catalysts prepared with full ion-exchange efficiency and with different H_2 treatment times is displayed with light-off curves in Fig. 5b. Full-Pd^{2+}/SSZ-13 exhibits a significantly lower catalytic activity compared to the thermal-treated Pd/SSZ-13 catalysts, indicating that the formation of PdO nanoparticles is required for CH_4 combustion. Importantly, the thermal-treated Pd/SSZ-13 catalyst prepared with full ion-exchange efficiency and with 5 min of H_2 treatment shows the highest CH_4 combustion activity. The CH_4 combustion activation barriers of the thermal-treated Pd/SSZ-13 catalysts range from 142 to 148 kJ mol^{-1}, consistent with the reported values of PdO in the Pd-impregnated zeolite catalysts (139–158 kJ mol^{-1}), whereas that of Full-Pd^{2+}/SSZ-13 is 241.7 kJ mol^{-1}, as displayed in Fig. 5c.[7,16] The similar activation barriers of the thermal-treated Pd/SSZ-13 catalysts indicate that the different activities between them are not attributed to the thermodynamic barrier. Considering that CH_4 combustion over the Pd-impregnated zeolite is reported to be a structure-insensitive reaction,[7,55,56] the different activities are ascribed to the phase homogeneity of Pd species as a PdO phase, and the dispersion of generated nano-sized PdO clusters. This explains our observation that the thermal-treated Pd/SSZ-13 catalyst with 5 min of H_2 treatment shows the most prominent CH_4 combustion activity due to the full conversion of isolated Pd^{2+} ions and the generation of size-focused nano-sized PdO clusters with high phase homogeneity. The low CH_4 combustion activity of the 1 min H_2-treated Pd/SSZ-13 catalyst can be explained by the insufficient conversion of isolated Pd^{2+} ions. Due to the
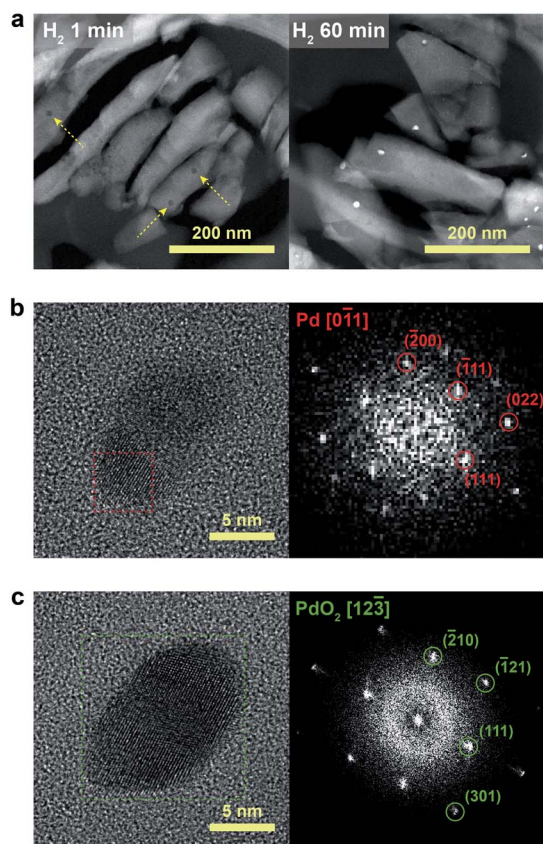

Fig. 4 (a) Cryo-STEM images of ultramicrotomed Pd/SSZ-13 catalysts with H_2 treatment times of 1 min and 60 min. Yellow arrows indicate the internal void sites. (b) and (c) Aberration-corrected TEM images and the selected-area fast Fourier transform (FFT) patterns of (b) Pd and (c) PdO_2 located at the internal void sites of the 60 min H_2-treated Pd/SSZ-13 catalyst.
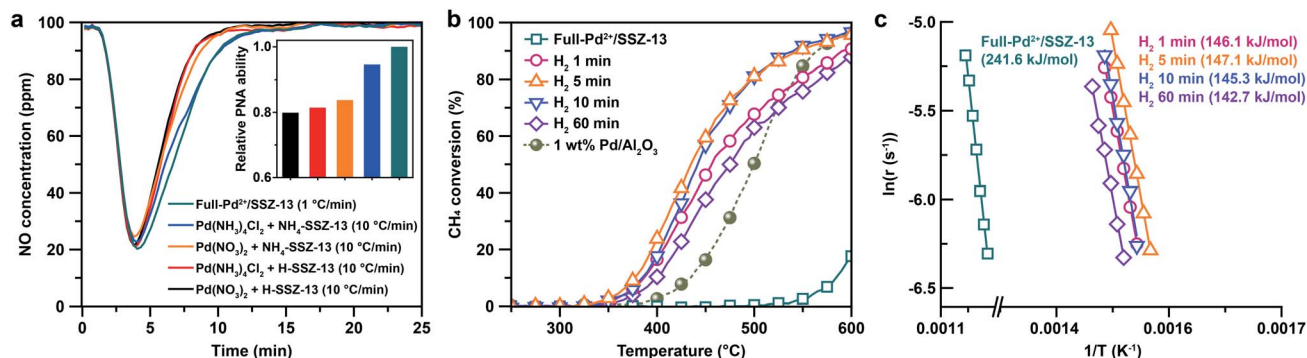
Fig. 5 (a) PNA ability of Pd-exchanged SSZ-13 catalysts prepared with different combinations of the Pd precursors, zeolite-forms, and ramping rates. (b) CH_4 combustion light-off curves and (c) Arrhenius plots of the Full-Pd^{2+}/SSZ-13 and thermal-treated Pd/SSZ-13 catalysts with different H_2 treatment times. The CH_4 combustion light-off curves of 1 wt% Pd/Al$_2$O$_3$ is also given in (b) for comparison.

similar size of PdO clusters in 5 min and 10 min of H_2 treatment, the CH_4 combustion activity of the 10 min H_2-treated Pd/SSZ-13 catalyst is similar to that of the 5 min H_2-treated Pd/SSZ-13 catalyst, but a minor reduction in 10 min was observed due to some agglomeration of Pd at the void site shown in Fig. S13.† Meanwhile, the increase of particle size and the development of unwanted Pd phases at the internal void site were clearly observed in the 60 min H_2-treated Pd/SSZ-13 catalyst, which explains the significantly reduced activity after 60 min of H_2 treatment. We also note that the CH_4 combustion activity of various Pd-exchanged SSZ-13 catalysts without thermal treatment (*i.e.* samples right after the calcination) shown in Fig. S17† is significantly low, compared to that of thermal-treated Pd/SSZ-13 catalysts shown in Fig. 5b.

The advantage of full ion-exchange before thermal treatment was further confirmed by comparing the catalytic activities of the thermal-treated Pd/SSZ-13 catalysts with the same H_2 treatment time of 5 min, but prepared using different combinations of Pd precursors and zeolite-forms. The light-off curves demonstrated that the thermal-treated Pd/SSZ-13 catalyst prepared from Full-Pd^{2+}/SSZ-13 shows the highest CH_4 combustion activity compared to the other thermal-treated Pd/SSZ-13 catalysts prepared with insufficient ion-exchange efficiency, as shown in Fig. S18.† In addition, the CH_4 combustion activation barriers of these catalysts were all found to be similar (Fig. S19†). Hence, the lower CH_4 combustion activity of the thermal-treated Pd/SSZ-13 catalysts prepared with insufficient ion-exchange efficiency is attributed to the pre-existence of large-sized PdO particles shown in Fig. S6,† which hinders the full conversion of isolated Pd^{2+} ions into the uniformly nano-sized PdO clusters.

Conclusions

In summary, based on the understanding of the ion-exchange process, the fully isolated Pd^{2+} ions in a small-pore SSZ-13 zeolite is achieved. Controlled thermal treatment of the fully isolated Pd^{2+}/SSZ-13 catalyst uniformly generates nano-sized PdO clusters with high phase homogeneity by rapid nucleation and suppressed nanoparticle growth, which is directly

investigated *via* advanced microscopic methods of cryo-STEM and ultramicrotomy. The maximized PNA and CH_4 combustion performances of the prepared Pd/SSZ-13 catalysts show that our study provides an efficient and practical route to uniformly disperse noble metal species in small-pore zeolites for various catalytic reactions, and introduces microscopic methods that can be widely applied in investigating zeolite-based catalysts.

Experimental

Chemicals

Sodium hydroxide (NaOH), sodium silicate (Ni$_2$SiO$_3$) solution, ammonium nitrate (NH$_4$NO$_3$), palladium nitrate dihydrate (Pd(NO$_3$)$_2$·2H$_2$O), and tetraamminepalladium chloride monohydrate (Pd(NH$_3$)$_4$Cl$_2$·H$_2$O) were purchased from Sigma-Aldrich. NH$_4$–Y zeolite (CBV500, Si/Al$_2$ = 5.2) was acquired from Zeolyst, and *N,N,N*-trimethyl-1-adamantylammonium hydroxide (TMAdaOH) was supplied by Sachem, Inc. Alumina (Al$_2$O$_3$) was obtained from Sasol.

Catalyst preparation

Synthesis of SSZ-13. SSZ-13 was synthesized according to our previous report and Zones' report.[30,57] In detail, NaOH solution (0.8 g of NaOH in 52 g of H$_2$O) was mixed with 25 g of Ni$_2$SiO$_3$ solution in a Teflon cup, and then stirred for 30 min. Thereafter, 2.5 g of Y-zeolite (CBV500) was added into the mixture and stirred for 30 min. To the resulting mixture, 10.5 g of 25 wt% TMAdaOH was added. The mixture was then stirred for another 30 min after which it was transferred to a stainless steel autoclave, and then heated in an oven at 140 °C for 4 days. The resulting powder was filtered, washed with deionized water, and subsequently dried overnight in an oven at 105 °C. To remove the organic agent, the powder was calcined at 550 °C for 8 h at a ramping rate of 1 °C min^{-1}, which resulted in Na-SSZ-13. NH$_4$-SSZ-13 was prepared by ion-exchanging Na-SSZ-13 in a 1 M NH$_4$NO$_3$ solution at 80 °C for 18 h, followed by filtration and drying. Ion-exchange with NH$_4$NO$_3$ was carried out twice. Furthermore, H-SSZ-13 was obtained *via* calcination of as-

synthesized NH_4-SSZ-13 under O_2 flowing conditions at 500 °C for 2 h at a ramping rate of 10 °C min^{-1}.

Conventional ion-exchange and calcination processes for preparing Pd-exchanged SSZ-13. Pd-exchanged SSZ-13 samples were prepared by conventional ion-exchange and calcination processes using different combinations of Pd precursors ($Pd(NO_3)_2$ and $Pd(NH_3)_4Cl_2$), zeolite-forms (H-SSZ-13 and NH_4-SSZ-13), and ramping rates for calcination. Particularly, 1 g of SSZ-13 was dispersed in 200 mL of a Pd solution containing an appropriate amount of the Pd precursor. The final Pd loading in the Pd-exchanged SSZ-13 was 1 wt%. The mixture was stirred at 80 °C for 18 h. The resulting powder was filtered and dried overnight at 105 °C. Notably, no Pd precursor was detected *via* $NaBH_4$ reduction in the solution resulting from filtration, indicating that all Pd precursors were ion-exchanged or adsorbed on SSZ-13. Finally, to decompose the Pd precursor, the product powder was calcined under O_2 flowing conditions at 500 C for 2 h. Typically, the ramping rate was 10 °C min^{-1}. However, because the ramping rate affects the extent of isolated Pd^{2+} ions after the calcination, the ramping rate was controlled to range from 1 °C min^{-1} to 50 °C min^{-1}. In particular, to prepare Full-Pd^{2+}/SSZ-13, the ramping rate was maintained at 1 °C min^{-1}.

Thermal treatment. Thermal treatment was performed on Pd-exchanged SSZ-13 for the nucleation and growth of Pd particles from isolated Pd^{2+} ions, and for the phase transition of metallic Pd into PdO. To achieve this, successive treatment that involved H_2 reduction and O_2 oxidation was carried out (Scheme S1†). Concretely, the Pd-exchanged SSZ-13 was heated to 700 °C with a ramping rate of 10 °C min^{-1} under N_2 flowing conditions. Then, it was exposed under 1 vol% H_2/N_2 flowing conditions at 700 °C, and to control the nucleation and growth process of Pd particles from the isolated Pd^{2+} ions, the exposure time was varied from 1 min to 60 min. Because some stable Pd^{n+} ions in the zeolite maintain their phases even at 550 °C under H_2 conditions, a high temperature of 700 °C was used to ensure the full conversion of Pd^{2+} ions to Pd particles.[58] Thereafter, the catalyst was cooled down to 500 °C under N_2 flowing conditions, and subsequently exposed to the 10 vol% O_2/N_2 flowing conditions for 30 min to oxidize metallic Pd to PdO. The ramping rate was 10 °C min^{-1} and only N_2 gas was flowed when ramping and cooling the temperature. Notably, since the O_2 treatment conditions were the same as the pretreatment conditions that were used before the reaction, such mild conditions would oxidize metallic Pd to PdO, but not regenerate isolated Pd^{2+} ions.[9,59]

Synthesis of Pd/Al_2O_3. Pd/Al_2O_3 was synthesized *via* the wet-impregnation method. First, 2 g of Al_2O_3 was dispersed in a $Pd(NO_3)_2$ solution and dried using a vacuum evaporator. The resulting powder was calcined under O_2 flowing conditions at 500 °C for 2 h at a ramping rate of 10 °C min^{-1}.

Characterization

Inductively coupled plasma atomic emission spectroscopy (ICP-AES). ICP-AES was carried out to determine the Pd loading of Pd-exchanged SSZ-13 samples using an Optima 4300DV spectrometer (PerkinElmer, USA).

Magic angle spinning nuclear magnetic resonance (MAS-NMR). ^{27}Al and ^{29}Si MAS-NMR spectra were obtained using a 500 MHz WB Bruker Advance II system with a 4 mm MAS probe. To obtain 512 time-averaged scans, the spinning frequency, spectral window, complex points, and pulse delay were maintained at 10 kHz, 65 kHz, 6572, and 0.1 s, respectively. The Si-to-Al ratio was calculated from the Si-NMR spectra. The Si-to-Al ratio was calculated from the Si-NMR spectra. In detail, Si-NMR was deconvoluted with different Si species based on the number of Al sharing oxygen. The Si-to-Al ratio was calculated by using the following equation suggested by Engelhardt *et al.*[60]

$$\frac{Si}{Al} = \frac{\sum_{n=0}^{4} I_{Si(nAl)}}{\sum_{n=0}^{4} 0.25n \times I_{Si(nAl)}}$$

where $I_{Si(nAl)}$ is the intensity of $Si(nAl)$ that shares n oxygens with Al.

X-ray diffraction (XRD). XRD patterns were acquired using a powder X-ray diffractometer (Smartlab, Rigaku) to investigate the zeolite structure with a voltage of 40 kV and a current of 30 mA. For high resolution, the scan speed and scanning step size were maintained at 1.0° min^{-1} and 0.2°, respectively.

Ultraviolet-visible (UV-vis) spectroscopy. Pd precursor solutions with similar concentrations used for ion-exchange were prepared. Thereafter, the UV-vis spectra of the Pd solutions were measured using a UV-vis spectrometer (U-5100, HITACHI).

Ultraviolet-visible diffuse reflectance spectroscopy (UV-vis DRS). Powder UV-vis DRS spectra were obtained using a Jasco V670 spectrometer at room temperature.

X-ray photoelectron spectroscopy (XPS). XPS analysis was performed using a K-alpha instrument (Thermo Scientific Inc., U.K.) equipped with Al Kα μ-focused monochromatic (1486.6 eV) at a current of 3 mA and voltage of 12 kV in the regions of C 1s, Si 2p, Al 2p and Pd 3d.

N_2 adsorption–desorption isotherms. The specific surface areas of samples were calculated based on the Brunauer–Emmett–Teller (BET) method from N_2 adsorption–desorption isotherms. The isotherms were collected at −196 °C using a BELSORP-mini II high-precision surface area and a pore size analyzer (BEL Japan Inc.). Before the analysis, the samples were degassed at 150 °C for 4 h to eliminate any contaminants and residual water. Since the vacuum condition at a temperature above 200 °C could form Pd particles that can block pores, the temperature was maintained at 150 °C.[59]

Ar adsorption–desorption isotherm. In order to obtain an average pore diameter of NH_4-SSZ-13, Ar adsorption–desorption was carried out using an ASAP 2020 (Micrometrics). Before the analysis, NH_4-SSZ-13 was evacuated at 300 °C for 4 h. Note that Ar molecules are more appropriate than N_2 molecules for the quantitative analysis such as the average pore diameter of small-pore zeolites.

Cryogenic hydrogen temperature-programmed reduction (cryo-H_2-TPR). Cryo-H_2-TPR was performed using BEL-CAT-II (BEL Japan Inc.) with a thermal conductivity detector (TCD). Before the analysis, the sample (0.03 g) was pretreated under O_2

conditions at 300 °C for 1 h with a ramping temperature of 10 °C min^{-1}. Thereafter, the sample was cooled to -90 °C and exposed to 5 vol% of H_2/Ar. The sample temperature was increased from -90 to 900 °C while recording the TCD signal.

X-ray absorption fine structures (XAFS). XAFS at the Pd K-edge were obtained from the 7D-XAFS beamline of the Pohang light source (PLS-II) at the Pohang accelerator laboratory (South Korea). A monochromator was a Si (111) crystal with a ring current of 300 mA and beam energy of 2.5 GeV. The X-ray signal of the Pd K-edge was collected at room temperature. The energies of incident (I_0) and fluorescence (I_f) beams were measured while purging ionization chambers with N_2 gas and calibrated by Pd-foil ($E_0 = 24\ 350$ eV). The step and duration times of the X-ray absorption near edge structure (XANES) and extended X-ray absorption fine structure (EXAFS) were 1.0 eV and 2 s, and 0.30 nm^{-1} and 3 s, respectively. The obtained data were processed using the Athena program (Demeter, U.S.A.).

TEM sample preparation, imaging, and analysis

To image the Pd species in SSZ-13, ultramicrotomy of the synthesized Pd/SSZ-13 catalysts was conducted. First, the synthesized Pd/SSZ-13 catalysts were dispersed in an epoxy resin, and then cured at 70 °C for more than 8 h. Thereafter, the resin-embedded catalysts were sliced into ~50 nm thick sections using an ultramicrotome (EM UC7, Leica) obtained from the National Instrumentation Center for Environmental Management (NICEM), Seoul National University. The ultra-microtomed sections were loaded onto carbon-deposited copper grids for further investigation.

TEM/STEM imaging of the Pd/SSZ-13 catalysts (either whole particle or sliced sections) was performed on a JEOL-2100F (JEOL Ltd) equipped with an UltraScan 1000XP CCP detector (Gatan) and a HAADF detector, under an acceleration voltage of 200 kV. Energy-dispersive X-ray spectroscopy (EDS) was performed and analyzed using the AZtecTEM software equipped in the same microscope. To image the ultramicrotomed Pd/SSZ-13 sections, STEM imaging at a cryogenic temperature of -180 °C was conducted using a cryo-transfer holder (Model 626, Gatan). High-resolution TEM images of Pd/SSZ-13 catalysts were obtained from JEOL-ARM200F (JEOL Ltd) equipped with a spherical aberration corrector in the objective lens and cold field emission gun, with an acceleration voltage of 80 kV. JEOL-ARM200F is installed at the National Center for Inter-university Research Facilities (NCIRF), Seoul National University.

We note that all the STEM images of the ultramicrotomed Pd/SSZ-13 catalysts presented in this study were obtained with a minimal application of scanning mode during the imaging, to further avoid the electron-beam induced damage. That is, the scanning mode was only applied at a low-magnification (typically 1/5 magnification of that of cryo-STEM images in Fig. 2c–f) to quickly search the sample of interest. At high-magnification where the images were collected for size quantification, the focus was adjusted outside the region of interest (ROI), and thus the Pd/SSZ-13 sections located in the ROI were scanned only once during the imaging.

To quantify the size of the nano-sized PdO clusters in cryo-STEM images, a homemade MATLAB algorithm was developed. Particularly, the pixel area of the individual nano-sized PdO clusters located at the internal pores of the zeolite was extracted *via* manual measurements and converted to nm.^{2} The diameter of the nano-sized clusters was mathematically calculated by assuming a spherical morphology of the measured nano-particles. After obtaining the particle size data of 500 nano-sized PdO clusters for each thermal-treated Pd/SSZ-13 catalyst, the kurtosis of size distribution was calculated based on the following equation:

$$\text{Kurt}[X] = E\left[\left(\frac{X - \mu}{\sigma}\right)^4\right]$$

where μ and σ are the average and the standard deviation of the distribution X, respectively. Notably, kurtosis represents the tailedness of the distribution, where the distribution with a high kurtosis value indicates a small development of tail. Therefore, it shows a sharp peak compared to the distribution with a similar standard deviation, but a lower kurtosis value.

Passive NO$_x$ adsorber (PNA) and CH$_4$ combustion

The catalytic performances of Pd/SSZ-13 catalysts for PNA and CH$_4$ combustion were evaluated using a packed bed reactor system. Particularly, 0.05 g of sieved Pd/SSZ-13 catalyst (150–180 μm) was loaded in a 1/2 inch quartz tubular reactor. To control the temperature of the reaction, a thermocouple was placed right above the sample. The feed gas was introduced through a 1/4 inch stainless line, and the line was heated at 120 °C to prevent condensation of water. The loaded catalyst was pre-treated under 10 vol% O_2 at 500 °C for 30 min. After the pretreatment, the temperature was cooled to 120 °C.

Various reactants such as O_2, H_2O, CO_2, CH_4, CO, and NO were introduced in the feed gas to simulate the realistic condition. Initially, to expose the catalyst under steam-containing conditions, 10 vol% O_2, 5 vol% H_2O 5 vol of CO_2, and balanced N_2 were added to the feed gas at 120 °C. After stabilizing for 30 min, 100 ppm of NO, 250 ppm of CO, and 1000 ppm of CH_4 were added to the feed gas. Therefore, the final feed gas contained 100 ppm NO, 250 ppm CO, 1000 ppm CH_4, 10 vol% O_2, 5 vol% H_2O, 5 vol% CO_2, and balance N_2. Notably, the total flowrate was maintained at 200 sccm in all cases.

After the catalyst was exposed to the final feed gas, the temperature was maintained at 120 °C for 20 min. During this period, to evaluate the PNA performance of the catalyst, the changes in the concentration of NO, NO_2, CO, and CH_4 were measured using an online FT-IR spectrometer (Nicolet iS-50, Thermo Scientific) with a 2 m gas cell. Specifically, the IR spectra were collected every 10 s *via* the IR series method to track the continuous changes in the concentrations of the reactants (Fig. S16†). The concentration of NO in the outlet gas was diminished under 100 ppm (the concentration in the feed gas) due to the adsorption of NO on the catalyst, and then slowly reached 100 ppm. The PNA performance of the catalyst was assessed based on the amount of adsorbed NO.

On the other hand, the CH$_4$ combustion activity was measured while ramping the temperature to 600 °C with a ramping rate of 5 °C min^{-1}. The concentrations of NO, NO$_2$, CO, and CH$_4$ in the outlet gas were measured again using an online FT-IR spectrometer.

The conversion and reaction rate of CH$_4$ during the reaction were calculated based on the following equations:

$$\text{CH}_4 \text{ conversion } (\%) = X_{\text{CH}_4} \ (\%) = \frac{C_{\text{CH}_4,\text{inlet}} - C_{\text{CH}_4,\text{outlet}}}{C_{\text{CH}_4,\text{inlet}}} \times 100$$

$$\text{Reaction rate } (\text{s}^{-1}) = r \ (\text{s}^{-1}) = \frac{C_{\text{CH}_4,\text{inlet}} \cdot v \cdot X_{\text{CH}_4}}{\left(\frac{\text{ML}}{\text{MW}}\right)}$$

where $C_{\text{CH}_4,\text{inlet}}$ is the inlet concentration of CH$_4$, $C_{\text{CH}_4,\text{outlet}}$ is the outlet concentration of CH$_4$ after the reaction, v is the volumetric flow rate, and X_{CH_4} is the conversion of CH$_4$. ML and MW are the Pd loading in the catalyst and the molecular weight of the Pd, respectively. Only the data where the X_{CH_4} value was below 20% were used for the Arrhenius plot.

The reliability of the catalyst preparation and reaction system was confirmed *via* a reproducibility and repeated test, as shown in Fig. S20.†

Author contributions

Yongwoo Kim: conceptualization, investigation, visualization, writing – original draft, and writing – review & editing. Jongbaek Sung: conceptualization, investigation, visualization, writing – original draft, and writing – review & editing. Sungsu Kang: writing – review & editing. Jaeha Lee: writing – review & editing. Min-Ho Kang: writing – review & editing. Sungha Hwang: writing – review & editing. Hayoung Park: writing – review & editing. Joodeok Kim: writing – review & editing. Younhwa Kim: writing – review & editing. Eunwon Lee: writing – review & editing. Gyeong-Su Park: methodology, and writing – review & editing. Do Heui Kim: supervision, conceptualization, funding acquisition, and writing – review & editing. Jungwon Park: supervision, conceptualization, funding acquisition, and writing – review & editing.

Conflicts of interest

There are no conflicts to declare.

Acknowledgements

References

1 Y. Chai, W. Shang, W. Li, G. Wu, W. Dai, N. Guan and L. Li, *Adv. Sci.*, 2019, **6**, 1900299.

2 M. Choi, Z. Wu and E. Iglesia, *J. Am. Chem. Soc.*, 2010, **132**, 9129–9137.

3 N. Wang, Q. Sun, R. Bai, X. Li, G. Guo and J. Yu, *J. Am. Chem. Soc.*, 2016, **138**, 7484–7487.

4 B. Wen, Q. Sun and W. M. H. Sachtler, *J. Catal.*, 2001, **204**, 314–323.

5 K. Khivantsev, N. R. Jaegers, L. Kovarik, J. C. Hanson, F. Tao, Y. Tang, X. Zhang, I. Z. Koleva, H. A. Aleksandrov, G. N. Vayssilov, Y. Wang, F. Gao and J. Szanyi, *Angew. Chem., Int. Ed.*, 2018, **57**, 16672–16677.

6 H. Xu, W. Chen, Q. Wu, C. Lei, J. Zhang, S. Han, L. Zhang, Q. Zhu, X. Meng, D. Dai, S. Maurer, A.-N. Parvulescu, U. Müller, W. Zhang, T. Yokoi, X. Bao, B. Marler, D. E. De Vos, U. Kolb, A. Zheng and F.-S. Xiao, *J. Mater. Chem. A*, 2019, **7**, 4420–4425.

7 J. B. Lim, D. Jo and S. B. Hong, *Appl. Catal., B*, 2017, **219**, 155–162.

8 Z. Wu, S. Goel, M. Choi and E. Iglesia, *J. Catal.*, 2014, **311**, 458–468.

9 Y. Ryou, J. Lee, S. J. Cho, H. Lee, C. H. Kim and D. H. Kim, *Appl. Catal., B*, 2017, **212**, 140–149.

10 J. G. McCarty, *Catal. Today*, 1995, **26**, 283–293.

11 Y.-H. Chen, C.-Y. Mou and B.-Z. Wan, *Appl. Catal., B*, 2017, **218**, 506–514.

12 J. Hwang, G. Kwak, Y.-J. Lee, Y. T. Kim, I. Jeong, S. Kim, K.-W. Jun, K.-S. Ha and J. Lee, *J. Mater. Chem. A*, 2015, **3**, 23725–23731.

13 E. Kang, H. Jung, J.-G. Park, S. Kwon, J. Shim, H. Sai, U. Wiesner, J. K. Kim and J. Lee, *ACS Nano*, 2011, **5**, 1018–1025.

14 P. Losch, W. Huang, O. Vozniuk, E. D. Goodman, W. Schmidt and M. Cargnello, *ACS Catal.*, 2019, **9**, 4742–4753.

15 J. de Graaf, A. J. van Dillen, K. P. de Jong and D. C. Koningsberger, *J. Catal.*, 2001, **203**, 307–321.

16 A. W. Petrov, D. Ferri, F. Krumeich, M. Nachtegaal, J. A. van Bokhoven and O. Kröcher, *Nat. Commun.*, 2018, **9**, 2545.

17 Y. Zheng, L. Kovarik, M. H. Engelhard, Y. Wang, Y. Wang, F. Gao and J. Szanyi, *J. Phys. Chem. C*, 2017, **121**, 15793–15803.

18 K. Manthiram, B. J. Beberwyck and A. P. Alivisatos, *J. Am. Chem. Soc.*, 2014, **136**, 13319–13325.

19 K. Manthiram, Y. Surendranath and A. P. Alivisatos, *J. Am. Chem. Soc.*, 2014, **136**, 7237–7240.

20 V. Ortalan, A. Uzun, B. C. Gates and N. D. Browning, *Nat. Nanotechnol.*, 2010, **5**, 506–510.

21 M. Juneau, R. Liu, Y. Peng, A. Malge, Z. Ma and M. D. Porosoff, *ChemCatChem*, 2020, **12**, 1826–1852.

22 O. Ugurlu, J. Haus, A. A. Gunawan, M. G. Thomas, S. Maheshwari, M. Tsapatsis and K. A. Mkhoyan, *Phys. Rev. B: Condens. Matter Mater. Phys.*, 2011, **83**, 113408.

23 S. X. Wang, L. M. Wang and R. C. Ewing, *J. Nucl. Mater.*, 2000, **278**, 233–241.

24 Z. Li, M. C. Johnson, M. Sun, E. T. Ryan, D. J. Earl, W. Maichen, J. I. Martin, S. Li, C. M. Lew, J. Wang, M. W. Deem, M. E. Davis and Y. Yan, *Angew. Chem., Int. Ed.*, 2006, **45**, 6329–6332.

25 Q. Chen, C. Dwyer, G. Sheng, C. Zhu, X. Li, C. Zheng and Y. Zhu, *Adv. Mater.*, 2020, **32**, 1907619.

26 J. R. Di Iorio, S. Li, C. B. Jones, C. T. Nimlos, Y. Wang, E. Kunkes, V. Vattipalli, S. Prasad, A. Moini, W. F. Schneider and R. Gounder, *J. Am. Chem. Soc.*, 2020, **142**, 4807–4819.

27 J. R. Di Iorio, C. T. Nimlos and R. Gounder, *ACS Catal.*, 2017, **7**, 6663–6674.

28 K. Mech, P. Żabiński, R. Kowalik and K. Fitzner, *Electrochim. Acta*, 2013, **104**, 468–473.

29 M. Benkhaled, S. Morin, C. Pichon, C. Thomazeau, C. Verdon and D. Uzio, *Appl. Catal., A*, 2006, **312**, 1–11.

30 J. Lee, J. Kim, Y. Kim, S. Hwang, H. Lee, C. H. Kim and D. H. Kim, *Appl. Catal., B*, 2020, **277**, 119190.

31 A. M. Beale, F. Gao, I. Lezcano-Gonzalez, C. H. F. Peden and J. Szanyi, *Chem. Soc. Rev.*, 2015, **44**, 7371–7405.

32 C. Stolz, A. Sauvage, P. Massiani and R. Kramer, *Appl. Catal., A*, 1998, **167**, 113–121.

33 H. Matsumoto and S. Tanabe, *J. Mater. Sci. Lett.*, 1992, **11**, 623–626.

34 T. M. Lardinois, J. S. Bates, H. H. Lippie, C. K. Russell, J. T. Miller, H. M. Meyer, K. A. Unocic, V. Prikhodko, X. Wei, C. K. Lambert, A. B. Getsoian and R. Gounder, *Chem. Mater.*, 2021, **33**, 1698–1713.

35 H. Jeong, J. Bae, J. W. Han and H. Lee, *ACS Catal.*, 2017, **7**, 7097–7105.

36 B. Liu, Y. Zheng, N. Hu, T. Gui, Y. Li, F. Zhang, R. Zhou, X. Chen and H. Kita, *Microporous Mesoporous Mater.*, 2014, **196**, 270–276.

37 J. Zecevic, G. Vanbutsele, K. P. de Jong and J. A. Martens, *Nature*, 2015, **528**, 245–248.

38 J.-O. Bovin, V. Alfredsson, G. Karlsson, A. Carlsson, Z. Blum and O. Terasaki, *Ultramicroscopy*, 1996, **62**, 277–281.

39 H. Wang, Y. Li, Y. Li, Y. Liu, D. Lin, C. Zhu, G. Chen, A. Yang, K. Yan, H. Chen, Y. Zhu, J. Li, J. Xie, J. Xu, Z. Zhang, R. Vilá, A. Pei, K. Wang and Y. Cui, *Nano Lett.*, 2019, **19**, 1326–1335.

40 Y. Li, Y. Li, A. Pei, K. Yan, Y. Sun, C.-L. Wu, L.-M. Joubert, R. Chin, A. L. Koh, Y. Yu, J. Perrino, B. Butz, S. Chu and Y. Cui, *Science*, 2017, **358**, 506–510.

41 K. Khivantsev, F. Gao, L. Kovarik, Y. Wang and J. Szanyi, *J. Phys. Chem. C*, 2018, **122**, 10820–10827.

42 K. Cheng, L. I. van der Wal, H. Yoshida, J. Oenema, J. Harmel, Z. Zhang, G. Sunley, J. Zečević and K. P. de Jong, *Angew. Chem., Int. Ed.*, 2020, **59**, 3592–3600.

43 X. Chen, Y. Cheng, C. Y. Seo, J. W. Schwank and R. W. McCabe, *Appl. Catal., B*, 2015, **163**, 499–509.

44 A. D. Benavidez, L. Kovarik, A. Genc, N. Agrawal, E. M. Larsson, T. W. Hansen, A. M. Karim and A. K. Datye, *ACS Catal.*, 2012, **2**, 2349–2356.

45 T. Epicier, S. Koneti, P. Avenier, A. Cabiac, A.-S. Gay and L. Roiban, *Catal. Today*, 2019, **334**, 68–78.

46 T. W. Hansen, A. T. DeLaRiva, S. R. Challa and A. K. Datye, *Acc. Chem. Res.*, 2013, **46**, 1720–1730.

47 L. Shang, T. Bian, B. Zhang, D. Zhang, L.-Z. Wu, C.-H. Tung, Y. Yin and T. Zhang, *Angew. Chem., Int. Ed.*, 2014, **53**, 250–254.

48 G. Prieto, J. Zečević, H. Friedrich, K. P. de Jong and P. E. de Jongh, *Nat. Mater.*, 2013, **12**, 34–39.

49 S. Zhang, M. Cargnello, W. Cai, C. B. Murray, G. W. Graham and X. Pan, *J. Catal.*, 2016, **337**, 240–247.

50 S. G. Kwon and T. Hyeon, *Small*, 2011, **7**, 2685–2702.

51 V. K. LaMer and R. H. Dinegar, *J. Am. Chem. Soc.*, 1950, **72**, 4847–4854.

52 F. Yin, S. Ji, P. Wu, F. Zhao and C. Li, *J. Catal.*, 2008, **257**, 108–116.

53 H. Xiong, K. Lester, T. Ressler, R. Schlögl, L. F. Allard and A. K. Datye, *Catal. Lett.*, 2017, **147**, 1095–1103.

54 M. Cargnello, V. V. T. Doan-Nguyen and C. B. Murray, *AIChE J.*, 2016, **62**, 392–398.

55 J.-H. Park, B. Kim, C.-H. Shin, G. Seo, S. H. Kim and S. B. Hong, *Top. Catal.*, 2009, **52**, 27–34.

56 G. Zhu, J. Han, D. Y. Zemlyanov and F. H. Ribeiro, *J. Am. Chem. Soc.*, 2004, **126**, 9896–9897.

57 S. I. Zones, *J. Chem. Soc., Faraday Trans.*, 1991, **87**, 3709–3716.

58 Y. Gu, R. P. Zelinsky, Y.-R. Chen and W. S. Epling, *Appl. Catal., B*, 2019, **258**, 118032.

59 J. Lee, Y. Ryou, S. Hwang, Y. Kim, S. J. Cho, H. Lee, C. H. Kim and D. H. Kim, *Catal. Sci. Technol.*, 2019, **9**, 163–173.

60 G. Engelhardt, U. Lohse, V. Patzelová, M. Mägi and E. Lippmaa, *Zeolites*, 1983, **3**, 233–238.